ADVANCED FUNCTIONAL MATERIALS
www.afm-journal.de

Impact of Hierarchical Dopant-Induced Microstructure on Thermoelectric Properties of p-Type Si-Ge Alloys Revealed by Comprehensive Multi-Scale Characterization

Kyuseon Jang, Won-Seok Ko, Ji-Hee Son, Jeong-In Jang, Bongseo Kim, Miquel Vega-Parades, Hanhwi Jang, Maryam Allahyari, Se-Ho Kim, KenHee Ryou, Donghyeon Chae, Hail Park, Yeon Sik Jung, Min-Wook Oh, Chanwon Jung, Christina Scheu,* and Pyuck-Pa Choi**

Dopant-induced microstructure in thermoelectric materials significantly affects thermoelectric properties and offers a potential to break the interdependence between electron and phonon transport properties. However, identifying all-scale dopant-induced microstructures and correlating them with thermoelectric properties remain a huge challenge owing to a lack of detailed microstructural characterization encompassing all length scales. Here, the hierarchical boron (B)-induced microstructures in B-doped $Si_{80}Ge_{20}$ alloys with different B concentrations are investigated to determine their precise effects on thermoelectric properties. By adopting a multi-scale characterization approach, including X-ray diffraction, scanning and transmission electron microscopy, and atom probe tomography, five distinctive B-induced phases within $Si_{80}Ge_{20}$ alloys are identified. These phases exhibit different sizes, compositions, and crystal structures. Furthermore, their configuration is comprehensively determined according to B doping concentrations to elucidate their consequential impact on the unusual changes in carrier concentration, density-of-states effective mass, and lattice thermal conductivity. The study provides insights into the intricate relationship between hierarchical dopant-induced microstructures and thermoelectric properties and highlights the importance of investigating all-scale microstructures in excessively-doped systems for determining the precise structure-property relationships.

1. Introduction

Owing to growing concerns on environmental pollution, the necessity for developing novel methods for generating clean energy is increasing rapidly.[1] Thermoelectric technology, which can be used to convert heat into electricity and vice versa, has been highlighted as a promising way to produce clean energy because of its low noise level and reliability.[2–5] The conversion efficiency of thermoelectric materials is indicated by their dimensionless figure-of-merit zT, which is given by $zT = \frac{S^2\sigma}{\kappa}T$, where S is the Seebeck coefficient, σ is the electrical conductivity, κ is the thermal conductivity, and T is the absolute temperature.[6] However, improving zT is highly challenging due to the interdependence between S, σ, and κ. Various approaches have been proposed to break this interdependency and increase the zT,[3] including doping,[7] nanostructuring,[8,9] band engineering,[10] and grain boundary modification.[11,12]

Among these approaches, doping via minor element alloying has traditionally

K. Jang, H. Jang, M. Allahyari, K. Ryou, D. Chae, H. Park, Y. S. Jung, P.-P. Choi
Department of Materials Science and Engineering
Korea Advanced Institute of Science and Technology (KAIST)
Daejeon 34141, Republic of Korea
E-mail: p.choi@kaist.ac.kr

The ORCID identification number(s) for the author(s) of this article can be found under https://doi.org/10.1002/adfm.202403785

© 2024 The Authors. Advanced Functional Materials published by Wiley-VCH GmbH. This is an open access article under the terms of the Creative Commons Attribution License, which permits use, distribution and reproduction in any medium, provided the original work is properly cited.

DOI: 10.1002/adfm.202403785

W.-S. Ko
Department of Materials Science and Engineering
Inha University
Incheon 22212, Republic of Korea

J.-H. Son, J.-I. Jang, B. Kim
Energy Conversion Research Center
Korea Electrotechnology Research Institute (KERI)
Changwon 51543, Republic of Korea

M. Vega-Parades, S.-H. Kim, C. Jung, C. Scheu
Max-Planck-Institut für Eisenforschung GmbH
40237 Düsseldorf, Germany
E-mail: c.jung@pknu.ac.kr; c.scheu@mpie.de

been the most popular to vary the carrier concentration and tune the thermoelectric properties.[13] Typically, the optimum carrier concentration for the highest zT in thermoelectric materials is in the range of 10^{19} to 10^{21} carriers cm^{-3},[3] corresponding to the range for degenerate semiconductors. However, dopant levels required for achieving the optimum carrier concentration in thermoelectric materials normally exceed the solubility limit, and they can cause the formation of dopant-rich secondary phases during material synthesis and processing, which are collectively referred to as "dopant-induced microstructure".[14] Such microstructures can have a size ranging from nanoscale to macroscale in parent materials.[14,15]

The beneficial impact of dopant-induced microstructures on thermoelectric properties has been reported for various thermoelectric materials, such as phase separation,[16] grain refinement,[17,18] precipitates,[19–21] texturing,[22] and grain boundary phases.[23,24] The dopant-induced microstructure can be exploited for designing advanced thermoelectric materials as it provides an additional parameter space to break the interdependence between electron and phonon transport. Furthermore, the presence of dopant-induced phases with different size scales can improve zT by effectively scattering phonons across a broad spectrum of wavelengths. It is imperative to comprehensively characterize such phases across all scales to understand the underlying origins of thermoelectric properties.[25] However, the multiscale natures of dopant-induced microstructures pose a significant challenge to their comprehensive analysis.

For instance, it is hard to obtain the accurate compositions and crystal structures of nanoscale features and figure out the configuration (i.e., number density and volume fraction) of all individual microstructures. These challenges can lead to issues where only a specific microstructure is considered in interpreting thermoelectric properties, or the impact of a particular microstructure is either exaggerated or underestimated. Such challenges hinder the establishment of a precise structure-property relationship in thermoelectric materials.[15] However, despite the critical importance of this task, a comprehensive analysis addressing these challenges is still lacking for thermoelectric materials.

In this work, we select boron (B-doped silicon-germanium (Si-Ge) alloys with different B concentrations as model systems to study the effect of the all-scale dopant-induced microstructure on thermoelectric properties. Si-Ge alloys show excellent thermoelectric performance and good chemical stability at temperatures above 1000 K.[8] B is a widely used p-type dopant for Si-Ge alloys, and many researchers have proposed that it is likely to have a heterogeneous distribution in Si-Ge alloys.[8,26–29] However, there is a lack of clarity on many aspects of B-doped Si-Ge alloys, such as the number of secondary phases that can coexist, the composition of the phases, the effect of the phases on the transport properties, and the distribution of B in the alloys. The lack of clarity is because of the difficulty in detecting and quantifying B owing to its low atomic mass and small atomic radius. Notably, an inexplicable discrepancy between experimentally observed properties and those determined through modeling by using the Boltzmann transport equation has been reported for B-doped Si-Ge alloys, and it could potentially be related to the effect of B-induced phases on the transport properties.[30] The aforementioned aspects are worth investigating since B is a widely used dopant for a variety of thermoelectric materials apart from Si-Ge alloys.[17,31–33]

Here, we identify the all-scale B-induced microstructures in nanostructured $Si_{80}Ge_{20}$ alloys for different B concentrations ($B_xSi_{80}Ge_{20}$, x = 0, 0.2, 1, 5, and 10) by using multi-scale material characterization techniques, including X-ray diffraction (XRD), scanning electron microscopy (SEM), scanning transmission electron microscopy (STEM), and atom probe tomography (APT). The complementary use of these techniques facilitated the investigation of all microstructural features of each of the detected phases (i.e., size, composition, density, volume fraction, crystal and interface structure), and the complete mapping of the B distribution in each $B_xSi_{80}Ge_{20}$ sample. The results show that five types of B-induced phases ranging from several nanometers to several micrometers in size can coexist and their configuration significantly varies with the B concentration. Importantly, these phases influence the thermoelectric transport properties, leading to their unusual changes with increasing B concentration. As a result, we demonstrate the complex structure-property relationships between the all-scale dopant-induced microstructures and transport properties.

2. Results and Discussion

2.1. Distinctive Changes in Thermoelectric Transport Properties with B Concentration

To investigate the effect of B on the thermoelectric transport properties, we first measured the electrical transport properties of $B_xSi_{80}Ge_{20}$ (x = 0, 0.2, 1, 5, and 10) samples. In **Figure 1a**, while the undoped sample (x = 0) shows minimal change in σ with temperature, the B-doped samples (x = 0.2, 1, 5, and 10) exhibit a monotonous decrease in σ with increasing temperature, which is a typical trend in degenerate semiconductors. The σ value of the $B_xSi_{80}Ge_{20}$ samples increased with B and saturated at x = 5. Meanwhile, the Hall carrier concentration (p_H) saturated at x = 1, hence the samples with x = 1, 5, and 10 showed nearly identical p_H values at room temperature (Figure 1b). A comparison of the measured p_H with the ideal p_H value (i.e., the p_H value obtained by assuming that all B atoms were ionized and generated holes) exhibited that the sample with x = 0.2 showed 100% doping efficiency while those with x = 1, 5, and 10 showed considerably low doping efficiency (31.1%, 6.8%, and 3.3%, respectively; Figure S1 and Table S1, Supporting Information).

The measured p_H values for x = 1, 5, and 10 were equivalent to the ideal p_H value when x = 0.28 (see Supporting Information). This result implies that the maximum amount of B atoms capable of generating charge carriers in $Si_{80}Ge_{20}$ is ≈0.28 at.%,

S.-H. Kim
Department of Materials Science and Engineering
Korea University
Seoul 02841, Republic of Korea
M.-W. Oh
Department of Materials Science and Engineering
Hanbat National University
Daejeon 34158, Republic of Korea
C. Jung
Department of Materials Science and Engineering
Pukyong National University
Busan 48513, Republic of Korea

© 2024 The Authors. Advanced Functional Materials published by Wiley-VCH GmbH
RIGHTSLINK
16163028, 2024, 40, Downloaded from https://onlinelibrary.wiley.com/doi/10.1002/adfm.202403785, Wiley Online Library on [23/10/2024]. See the Terms and Conditions (https://onlinelibrary.wiley.com/terms-and-conditions) on Wiley Online Library for rules of use; OA articles are governed by the applicable Creative Commons License

16163028, 2024, 40, Downloaded from https://onlinelibrary.wiley.com/doi/10.1002/adfm.202403785, Wiley Online Library on [23/10/2024]. See the Terms and Conditions (https://onlinelibrary.wiley.com/terms-and-conditions) on Wiley Online Library for rules of use; OA articles are governed by the applicable Creative Commons License

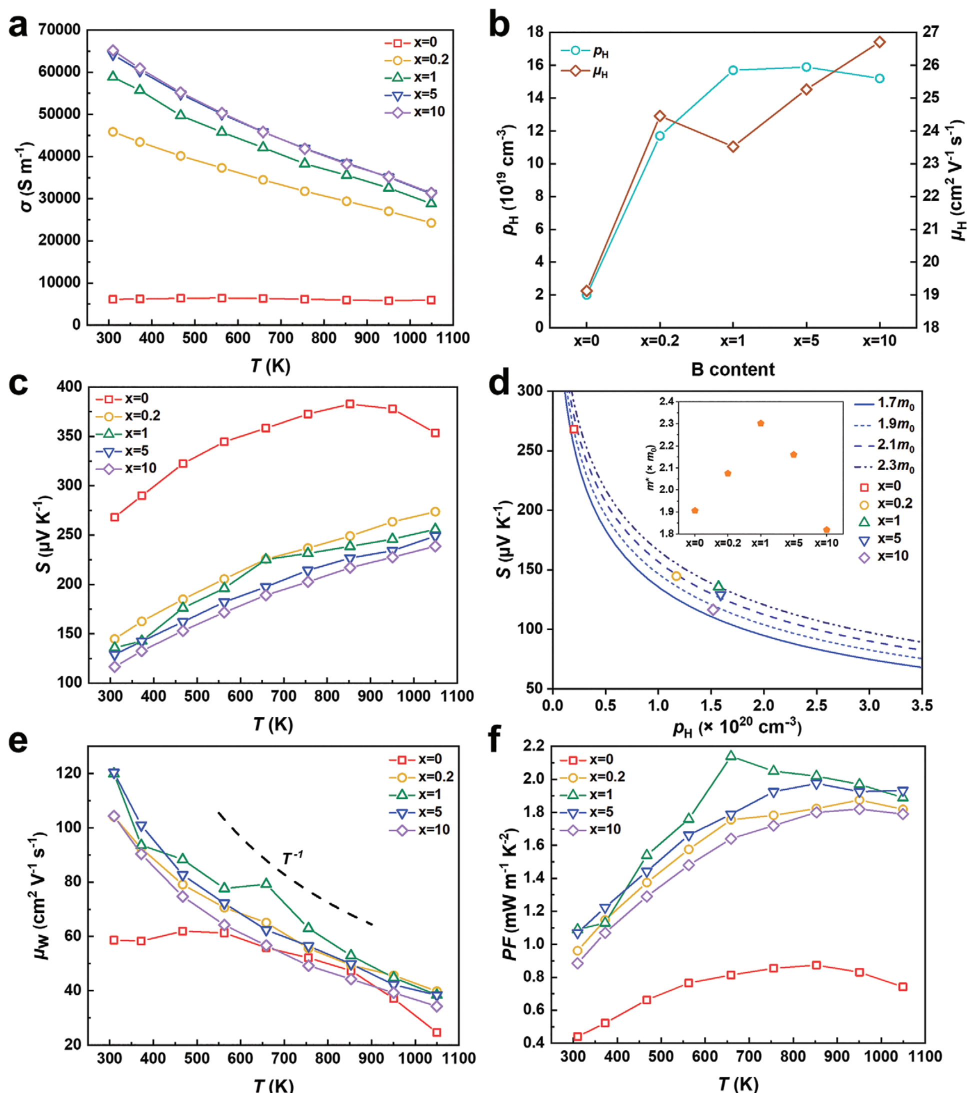

Figure 1. Electrical transport properties of $B_xSi_{80}Ge_{20}$. a) Electrical conductivity (σ), b) Hall carrier concentration (p_H) and Hall mobility (μ_H) at 298 K, c) Seebeck coefficient (S), d) Pisarenko plot at 298 K based on the single parabolic band model, e) weighted mobility (μ_w), and f) power factor (PF) of $B_xSi_{80}Ge_{20}$ ($x = 0$, 0.2, 1, 5, and 10) samples. The inset in (d) shows the density-of-states (DOS) effective mass (m^*) of each sample obtained from the Pisarenko plot; m_0 denotes the electron mass.

slightly exceeding the reported solubility limit of B (≈0.2 at.%) in Si at room temperature.[34] This value can be attributed to the ball milling process, which introduces a large number of defects that facilitate alloying with high B content.[35] Therefore, the excess amount of B above 0.28 at.% is insoluble in the $Si_{80}Ge_{20}$ matrix and cannot act as an acceptor to generate holes. However, without any detailed microstructural characterization, it remains unclear in which phases such residual B atoms exist in $Si_{80}Ge_{20}$.

The Hall mobility (μ_H) also showed an unusual trend with increasing B. It first increased with B up to $x = 0.2$, slightly decreased for $x = 1$, and again increased thereafter, with the increase continuing at $x = 5$ and 10 (Figure 1b). The increase in μ_H between $x = 0$ and 0.2 was atypical, as μ_H generally decreases with increasing p_H owing to strong ionized impurity scattering.[36] A similar atypical increase has been reported for B-, P-, and $NaBH_4$-doped $Si_{80}Ge_{20}$ alloys.[28,37,38] This behavior can be explained by the change in the deformation potential (E_{def}), which indicates the strength of carrier scattering by the acoustic phonons[39] (see Supporting Information). Notably, the sample with $x = 0.2$ exhibits a lower E_{def} compared to $x = 0$, suggesting that B doping attenuates the electron-phonon coupling (Figure S2, Supporting Information). This lower E_{def} observed for $x = 0.2$ accounts for the higher μ_H in $x = 0.2$ than in $x = 0$ despite its higher n_H. However, the lowest μ_H observed for $x = 1$ and the slight increment of μ_H for $x = 5$ and 10 cannot be explained solely by the change in E_{def}. This trend can be related to changes in the microstructure or band structure.

For the $B_xSi_{80}Ge_{20}$ samples, S exhibited a monotonous increase with increasing temperature, while for $x = 0$, it decreased above 873 K due to the bipolar effect (Figure 1c). This was confirmed from high-temperature Hall measurements. For $x = 0$, p_H increased at 1073 K compared to 298 K by thermal activation

© 2024 The Authors. Advanced Functional Materials published by Wiley-VCH GmbH
RIGHTSLINK

16163028, 2024, 40, Downloaded from https://onlinelibrary.wiley.com/doi/10.1002/adfm.202403785, Wiley Online Library on [23/10/2024]. See the Terms and Conditions (https://onlinelibrary.wiley.com/terms-and-conditions) on Wiley Online Library for rules of use; OA articles are governed by the applicable Creative Commons License

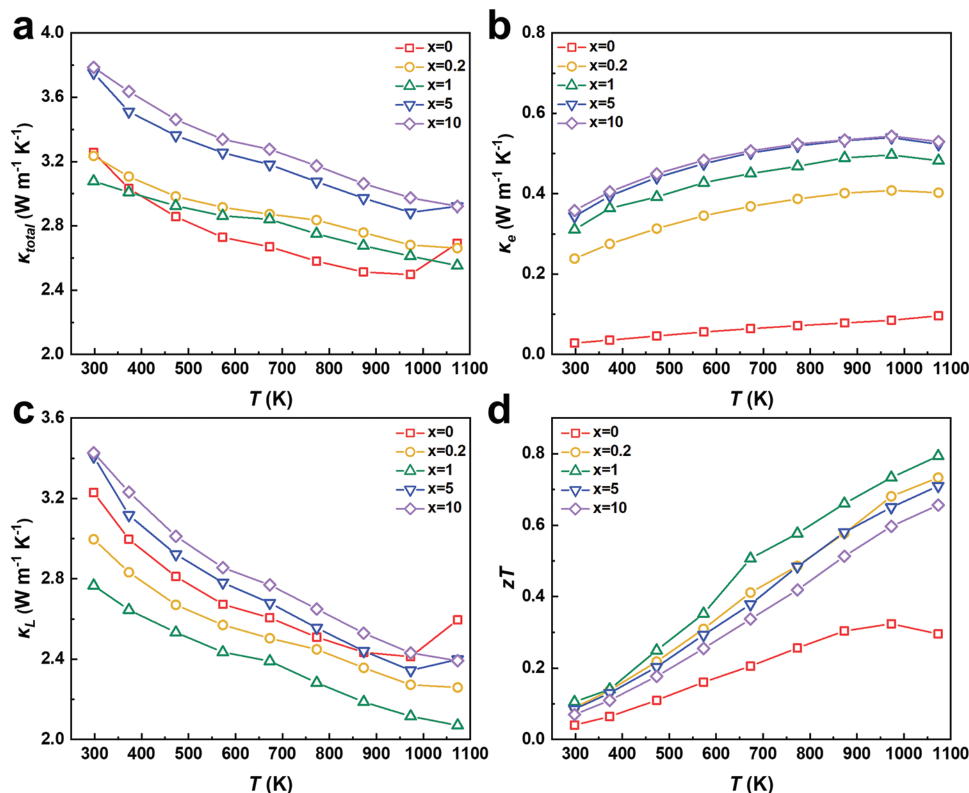

Figure 2. Thermal transport and thermoelectric properties of $B_xSi_{80}Ge_{20}$. a) Total thermal conductivity (κ_{total}), b) electronic thermal conductivity (κ_e), c) lattice thermal conductivity (κ_L), and d) figure-of-merit (zT) of $B_xSi_{80}Ge_{20}$ ($x = 0$, 0.2, 1, 5, 10) samples.

(Figure S3, Supporting Information). By contrast, the other samples showed almost identical p_H values at 298 and 1073 K. Since S is inversely proportional to carrier concentration according to the Pisarenko relation, the largest S was observed for $x = 0$ and the smallest values were expected for $x = 1$, 5, and 10.[40] However, the sample with $x = 1$ showed a larger S value than those with $x = 5$ and 10, despite the identical p_H values. This difference originated from the different density-of-states (DOS) effective mass (m^*). The m^* of each sample was determined from the Pisarenko plot based on the single parabolic band (SPB) model (see Supporting Information). We assumed that acoustic phonon scattering is the dominant carrier scattering in all $B_xSi_{80}Ge_{20}$ samples across the entire temperature range, based on the results of the Kang-Snyder model (see Supporting Information and Figure S4, Supporting Information).[41] As shown in the Pisarenko plot in the inset of Figure 1d, m^* increased from $x = 0$ to $x = 1$, but decreased for $x = 5$ and 10. The largest m^* value of $2.3m_0$ was measured for $x = 1$. This significant increase in m^* for $x = 1$ counteracts the advantageous effect of its E_{def} on μ_H, thereby resulting in its lower μ_H compared to other B-doped $Si_{80}Ge_{20}$ samples. Accordingly, the smaller μ_H and higher S of the sample with $x = 1$ compared with those of the samples with $x = 5$ and 10 are ascribed to its larger m^*. Such nonlinear change in m^* could have resulted from the alteration in the band structure induced by either B doping or the formation of the B-induced microstructure.

We also calculated the weighted mobility (μ_w) by using σ and S to identify the intrinsic scattering mechanism of each sample (see Supporting Information). For the samples with $x = 0.2$, 1, 5, and 10, μ_w decreased with increasing temperature, and all samples showed similar T^{-1} dependence. This observation indicated the insignificant difference in the electron scattering mechanism between the B-doped $Si_{80}Ge_{20}$ samples. The T^{-1} dependence showed mixed electron scattering by acoustic phonon scattering ($\mu_w \propto T^{-3/2}$) and point defect scattering ($\mu_w \propto T^{-1/2}$).[42] By contrast, μ_w for the sample with $x = 0$ showed thermally activated behavior up to 500 K, could be attributed to the grain boundary scattering. Furthermore, the sample with $x = 1$ showed the highest μ_w, unlike μ_H, since it had the largest m^*; μ_w is given by[43]

$$\mu_w = \mu_H \left(\frac{m^*}{m_0}\right)^{3/2} \tag{1}$$

Because of the combination of high σ and high S resulting from the large m^*, the sample with $x = 1$ had the highest power factor (PF) (Figure 1f).

In addition to p_H and m^*, anomalous changes resulting from B addition were also observed in the thermal transport properties (**Figure 2**). The samples with $x = 0.2$ and 1 showed similar total thermal conductivity (κ_{total}) values, while those with $x = 5$ and 10 showed higher κ_{total} values (Figure 2a). Except for the sample with $x = 0$, no sample showed the bipolar effect at high temperatures. The parameter κ_{total} can be decomposed into electronic (κ_e) and lattice (κ_L) contributions by using the Wiedemann–Franz law, as expressed in the following equation:

$$\kappa_e = L\sigma T, \quad \kappa_L = \kappa_{total} - \kappa_e \tag{2}$$

© 2024 The Authors. Advanced Functional Materials published by Wiley-VCH GmbH
RIGHTSLINK

where the bipolar effect is not considered. Lorenz number, L was calculated using the SPB model assuming that acoustic phonon scattering is dominant (see Supporting Information)

In accordance with Equation (2), κ_e follows the same trend as σ, namely, it increased with the B content and reached saturation at $x = 5$ (Figure 2b). However, κ_L showed an unexpected trend; the sample with $x = 1$ had the lowest κ_L, and the samples with $x =$ 5 and 10 had much higher κ_L values (Figure 2c). The lower κ_L for $x = 0.2$ compared with κ_L for $x = 0$ can be explained by phonon scattering induced by substitutional B atoms in the $Si_{80}Ge_{20}$ matrix. Similarly, the lower κ_L for $x = 1$ compared with κ_L for $x =$ 0.2 can be attributed to stronger phonon scattering from higher B concentration. However, this cannot explain why the samples with $x = 5$ and 10 showed much higher κ_L than that with $x = 1$, despite all three samples having identical p_H. These results suggest that the B-induced microstructure associated with residual B affects κ_L of the samples with $x = 1$, 5, and 10 differently, underscoring the need for a comprehensive microstructure analysis to understand such behavior.

The combination of high μ_w and low κ_L positioned $x = 1$ as the optimal B doping concentration with the highest thermoelectric quality factor (see Supporting Information and Figure S5, Supporting Information).[31] Consequently, $x = 1$ yielded the highest maximum zT value (≈0.8) across the entire temperature range (Figure 2d) with the largest average zT value (≈0.5) (Figure S6, Supporting Information). The zT values of $B_xSi_{80}Ge_{20}$ samples in this study show comparable zT values with the other reported B-doped $Si_{80}Ge_{20}$ systems, surpassing the zT values of $Si_{80}Ge_{20}$ samples used in NASA RTG owing to their lower κ_{total} (Figure S7, Supporting Information).[8] Moreover, previous studies have suggested that the incorporation of additional composites such as Ga_2O_3, SiO_2, B_2O_3, and WSi_2 can further enhance the zT values of $B_xSi_{80}Ge_{20}$ systems.

2.2. Identification of B-Induced Phases at Microscale and Macroscale

To understand the microstructural origins of the distinctive changes in thermoelectric transport properties (i.e., p_H saturation and unexpected variations in m^* and κ_L in the samples with $x = 1$, 5, and 10), we conducted XRD and SEM analyses. In **Figure 3a**, the main peaks can be assigned to the Si-Ge alloy and no additional peaks were observed for $x = 0$ and 0.2. However, for $x \geq 1$, additional peaks of low intensity appeared at higher 2θ values next to the Si-Ge alloy peaks, as evident in the magnified patterns in Figure 3a. The additional peaks can be ascribed to a secondary phase that has the same crystal structure as the Si-Ge alloy but with a smaller lattice constant.

The lattice constants of the B-doped $Si_{80}Ge_{20}$ samples (i.e., $x =$ 0.2, 1, 5, and 10) were smaller than that of the sample with $x =$ 0, indicating that lattice contraction occurred because of substitutional B atoms in the Si-Ge lattice due to its smaller atomic radius (87 pm) than Si (110 pm) and Ge (125 pm) (Figure 3b). This assertation is corroborated by density functional theory (DFT) calculations by modeling the B-doped $Si_{80}Ge_{20}$ ($B_{2x}Si_{80-x}Ge_{20-x}$) alloys based on special quasi-random structures (SQS) (see Supporting Information). The DFT calculations reveal that the lattice parameter of B-doped $Si_{80}Ge_{20}$ alloys linearly decreases with increasing B concentration (Figure S8, Supporting Information). However, the lattice constants of the Si-Ge matrix were almost identical for $x = 0.2$, 1, 5, and 10. This implies that differences in the matrix B concentration among the samples were insignificant, in agreement with the Hall measurements (Figure 1b). The secondary phase had a smaller lattice constant (≈5.425 Å) than the Si-Ge matrix (≈5.468 Å), and it was even smaller than the pure Si samples (5.431 Å) fabricated by the same process as $B_xSi_{80}Ge_{20}$ (see Experimental Section). This finding indicates that the secondary phase was not pure Si, but a mixture of Si and a small amount of B; B caused the Si lattice to contract.[44] The volume fraction of the secondary phase for $x = 1$, 5, and 10, determined by using the XRD peak integration method, was almost identical (≈2.4 vol.%) for $x = 1$, 5, and 10 (Figure S9, Supporting Information). Therefore, the secondary phase could not fully explain how residual B atoms were present in the $B_xSi_{80}Ge_{20}$ samples, and this implies that different types of B-induced phases or B-enriched defects, which were not detected by XRD, were present.

The presence of B-induced phases for $x = 1$, 5, and 10 was confirmed by SEM analyses (Figure 3c–g). While the samples with $x = 0$ and 0.2 had homogeneous surfaces without any precipitates, dark-contrast precipitates were formed on the samples with $x = 1$, 5, and 10. These precipitates showed a dark contrast in backscattered electron (BSE) images (Figure S10, Supporting Information), indicating the presence of elements with a lower average atomic number than the Si-Ge matrix. Furthermore, some precipitates showed a darker contrast than others in BSE images, suggesting the presence of different precipitate types on the surface. Notably, the number density of these precipitates increased with the nominal B concentration (Figure 3h), but their average sizes did not change significantly (1.35 ± 0.98, 0.99 ± 0.84, and 1.04 ± 1.00 µm for $x = 1$, 5, and 10, respectively). This result implies that residual B atoms increased the number of precipitates rather than the precipitate size. The size distributions of the precipitates are well represented by log-normal distribution (Figure 1h).

The composition of the matrix and precipitates was investigated by using energy-dispersive X-ray spectroscopy (EDS). The composition of the matrix closely matched the nominal value ($Si_{80}Ge_{20}$) for every sample (Figure S11, Supporting Information). Precipitates with different contrasts in BSE images were categorized into two types based on their EDS spectra. While precipitates with less dark contrast showed a strong Si peak without any Ge and B peaks in their EDS spectra, those with darker contrast exhibited a very strong B peak and minor O, Mg, and Si peaks (Figure S11, Supporting Information). Since additional peaks in XRD patterns were expected for the mixture of Si with a trace amount of B, precipitates with less dark contrast (hereafter referred to as Si(B) phase) were presumed to be the secondary phase detected by XRD, while B was not detected by SEM-EDS owing to its low concentration. By contrast, the precipitates with darker contrast were identified as B inclusions. However, it was difficult to determine their exact composition because of the insensitivity of EDS to light elements. To determine their composition and why such B inclusions were not detected by XRD, we performed further analyses by STEM and APT.

© 2024 The Authors. Advanced Functional Materials published by Wiley-VCH GmbH

16163028, 2024, 40, Downloaded from https://onlinelibrary.wiley.com/doi/10.1002/adfm.202403785, Wiley Online Library on [23/10/2024]. See the Terms and Conditions (https://onlinelibrary.wiley.com/terms-and-conditions) on Wiley Online Library for rules of use; OA articles are governed by the applicable Creative Commons License
RIGHTSLINK

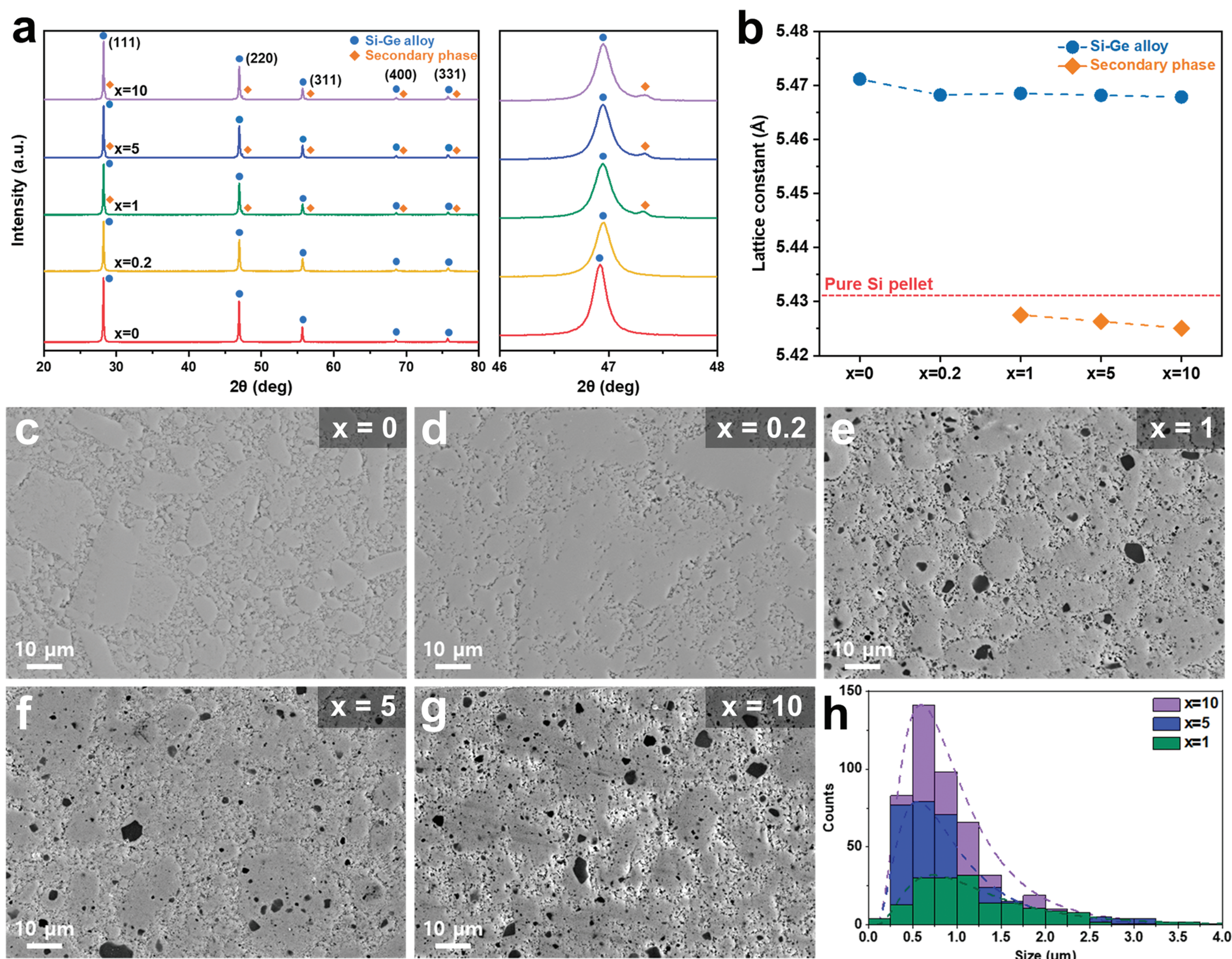

Figure 3. Evolution of microstructure induced by B. a) XRD patterns of the $B_xSi_{80}Ge_{20}$ (x = 0, 0.2, 1, 5, and 10) samples. b) Lattice constants of Si-Ge alloy (purple) and secondary phase (orange) of $B_xSi_{80}Ge_{20}$ calculated from the XRD peaks. The dotted line shows the lattice constants of pure Si pellet fabricated using the same procedure as that employed for preparing $B_xSi_{80}Ge_{20}$. c–g) Surface SEM images of $B_xSi_{80}Ge_{20}$ samples. h) Size distribution of dark precipitates observed in the samples with x = 1, 5, and 10. Dashed curves show log-normal distributions.

2.3. Identification of B-Induced Nanoprecipitates through STEM and APT

STEM analyses were conducted to detect the presence of nanoscale B-induced phases and ascertain the crystal structure of each phase. **Figure 4** presents representative STEM-EDS results for the hierarchical B-induced microstructure for the sample with $x = 1$. In Figure 4a, the phase with darker contrast showed a high-intensity Si signal in EDS maps (Figure 4b) and it corresponded to the Si(B) phase. However, the B signal was hardly distinguishable owing to the low B concentration in Si(B). The size of the Si(B) phases, detected in multiple TEM specimens for different samples, ranged between 2 and 4 µm. Figure 4c shows a phase with a strong B signal and Si and Ge are absent in the corresponding EDS maps (Figure 4d); these observations indicate that the phase corresponds to B inclusion detected in the SEM-EDS analyses. In the EDS spectrum of this region, distinct B peaks and Mg peaks were observed (Figure S12, Supporting Information). The presence of Mg in the B inclusion can be attributed to Mg impurities in the raw B powder, as the amorphous B powder was prepared through the reduction of B_2O_3 with Mg.[45]

The size range of the B inclusion was mostly ≈0.5 to 2 µm as observed using STEM; thus, it was smaller than the Si(B) regions. Besides Si(B) and B inclusions, silicon oxide (SiO_x) particles were identified through STEM-EDS analyses (Figure 4e,f). Although we conducted ball milling and spark plasma sintering (SPS) in a vacuum, nanoscale SiO_x particles with sizes ranging from 5–50 nm were formed because of the presence of oxygen in the raw materials or low vacuum (≈10^{-2} to 10^{-3} Torr) of the SPS chamber.[46,47] Such oxygen contamination is hardly avoidable given the ubiquitous nature of oxygen and the high oxygen affinity of Si. Residual oxygen has been consistently observed in a variety of sintered $Si_{80}Ge_{20}$ samples prepared using different techniques, such as induction melting, gas atomization, and pulverization.[48] In Si-Ge alloys, the formation of SiO_x particles is well-documented, and these particles are recognized for their

© 2024 The Authors. Advanced Functional Materials published by Wiley-VCH GmbH

16163028, 2024, 40, Downloaded from https://onlinelibrary.wiley.com/doi/10.1002/adfm.202403785, Wiley Online Library on [23/10/2024]. See the Terms and Conditions (https://onlinelibrary.wiley.com/terms-and-conditions) on Wiley Online Library for rules of use; OA articles are governed by the applicable Creative Commons License

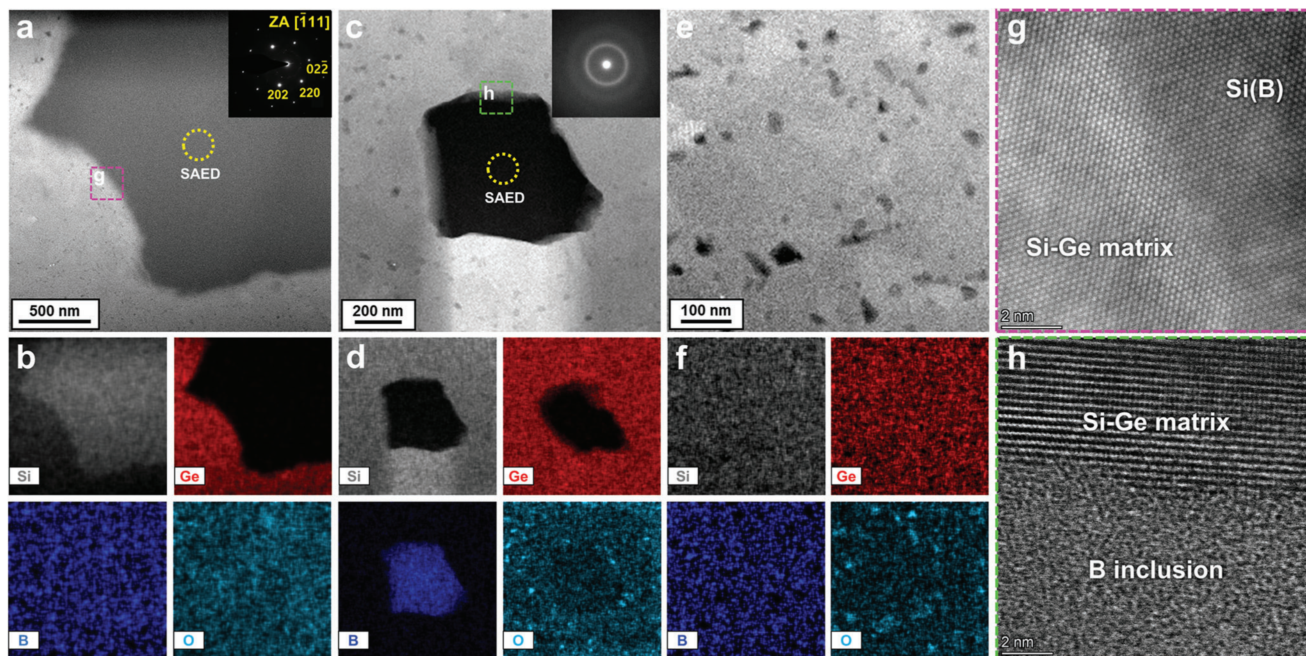

Figure 4. STEM-EDS analysis for hierarchical B-induced phases in the sample with $x = 1$. High-angle annular dark-field (HAADF)-STEM images and corresponding EDS maps of a,b) the Si(B) phase, c,d) B inclusion, and e,f) silicon oxide (SiO_x) particles. The insets in (a) and (c) show selected area electron diffraction (SAED) patterns of the Si(B) phase and B inclusion in the regions within the dotted yellow circles, respectively. g,h) High-resolution STEM images of (g) the interface between the Si(B) phase (HAADF image) and the Si-Ge matrix and (h) the interface between B inclusion and the Si-Ge matrix (ADF image) captured from the dotted squares in (a) and (c).

dual effect of reducing the κ_L of the alloys while simultaneously decreasing the σ due to their insulating properties.[49] Similar B-induced microstructures (i.e., Si(B), B inclusions, and SiO_x) were observed in the samples with $x = 5$ and 10 (Figure S13, Supporting Information). By contrast, no B-induced phases were observed for $x = 0$ and 0.2, as expected from their SEM images, but nanoscale SiO_x particles were presented in both samples (Figure S14, Supporting Information).

Furthermore, we investigated the crystal and interface structure of Si(B), B inclusions, and SiO_x as both factors influence thermoelectric properties by altering the scattering behavior of precipitates for carriers and phonons. The selected area electron diffraction (SAED) pattern showed that the Si(B) phase had the same crystal structure as the Si-Ge matrix, consistent with the XRD results (inset of Figure 4a). Furthermore, the Si(B) phase shared a identical zone axis with the adjacent matrix, and hence, it had a coherent interface with the matrix (Figure 4g). By contrast, the B inclusion had an amorphous structure, indicated by a diffuse ring in the SAED pattern (inset of Figure 4c); therefore, it had an amorphous-crystalline interface with the matrix (Figure 4h). This result explains why B inclusions were not detected by XRD.

There have been conflicting observations regarding the crystal structure of SiO_x particles in Si-Ge alloys in previous studies (i.e., whether they have an amorphous or crystalline structure).[50,51] We employed 4D-STEM to investigate the crystal structure of the SiO_x particles since their size was too small to obtain a standalone SAED pattern. The pixelated detection of diffraction patterns by using a nanoprobe in 4D-STEM facilitated the investigation of the crystal structure of individual nanosized SiO_x particles. The nanobeam diffraction patterns obtained from three points around SiO_x for $x = 1$ are shown in Figure S15 (Supporting Information). As the points approached the SiO_x particles, the diffraction pattern showed a diffuse ring apart from reflections of the surrounding Si-Ge matrix. This result indicates the amorphous nature of our SiO_x particles, in agreement with the observation of Bernard-Granger et al.[50] The mixed pattern of a diffuse ring and diffraction spots was formed since the thickness of the TEM lamella caused the overlap of the SiO_x particle signal and surrounding Si-Ge matrix. The SiO_x particles also had an amorphous-crystalline interface with the matrix, similar to the B inclusion. No other nanoscale precipitate was found to have a crystalline structure in the 4D-STEM analyses.

Next, APT was used to investigate the composition and distribution of B in each phase. APT is an advanced analytical technique used for 3D, atomic-scale material analysis. It is capable of quantitatively analyzing all elements regardless of their atomic mass, including light elements such as B and O, with a sensitivity at the parts-per-million level.[52,53] The APT results confirmed that Si(B) indeed contained a very small amount (≈0.15 at.%) of B ($Si_{99.85}B_{0.15}$) and the B inclusion primarily consisted of B along with ≈4 at.% of Mg impurities, consistent with the STEM-EDS results (Figure S16, Supporting Information).

We identified additional B-induced nanoprecipitates from the APT results. **Figure 5** presents the 3D atom maps of $B_xSi_{80}Ge_{20}$ ($x = 0.2$, 1, 5, 10) samples, showing the spatial distribution of B. For $x = 0.2$, most of the atom maps revealed a homogeneous B distribution (Figure 5a). However, some APT maps of the sample with $x = 0.2$ revealed small B clusters ≈10 nm in size (Figure S17, Supporting Information), which could be attributed to local

© 2024 The Authors. Advanced Functional Materials published by Wiley-VCH GmbH
RIGHTSLINK
16163028, 2024, 40, Downloaded from https://onlinelibrary.wiley.com/doi/10.1002/adfm.202403785, Wiley Online Library on [23/10/2024]. See the Terms and Conditions (https://onlinelibrary.wiley.com/terms-and-conditions) on Wiley Online Library for rules of use; OA articles are governed by the applicable Creative Commons License

16163028, 2024, 40, Downloaded from https://onlinelibrary.wiley.com/doi/10.1002/adfm.202403785, Wiley Online Library on [23/10/2024]. See the Terms and Conditions (https://onlinelibrary.wiley.com/terms-and-conditions) on Wiley Online Library for rules of use; OA articles are governed by the applicable Creative Commons License

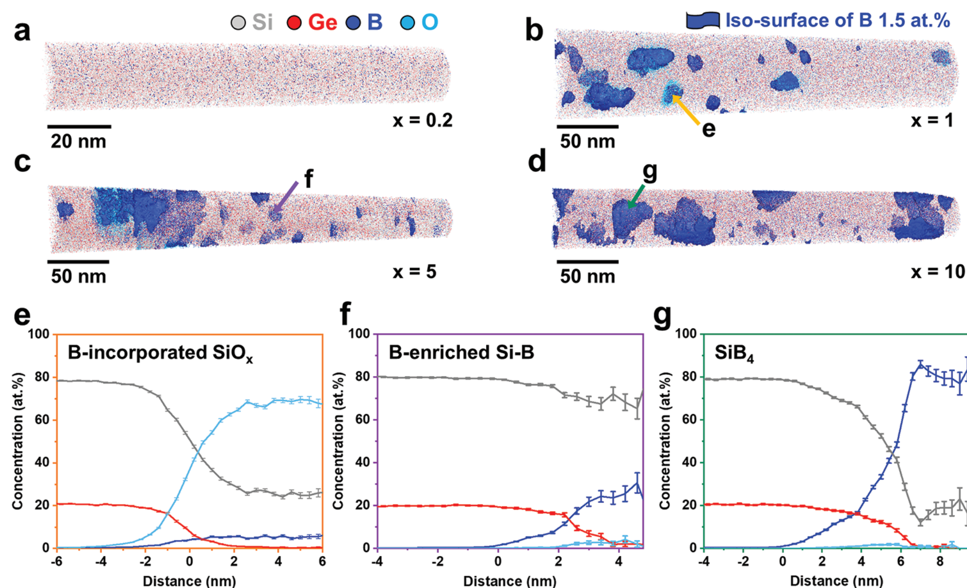

Figure 5. APT results for $B_xSi_{80}Ge_{20}$ (x = 0.2, 1, 5, 10). 3D atom maps of the samples with a) x = 0.2, b) x = 1, c) x = 5, and d) x = 10 with an iso-concentration surface of 1.5 at.% B. e–g) Proximity histograms of the three different B-induced nanoprecipitates marked by arrows in the atom maps. (e) B-incorporated SiO_x, (f) B-enriched Si-B, and (g) equilibrium SiB_4 precipitates.

compositional fluctuations of B beyond its solubility limit (i.e., 0.28 at.%) in the matrix during the synthesis. Since the p_H of x = 0.2 matched the ideal p_H (Figure S1, Supporting Information), the B clusters was considered to have a negligible impact on p_H and thermoelectric properties. For x = 1, 5, and 10, a highly heterogeneous distribution of B was evident from 1.5 at.% B iso-concentration surfaces (see Figure 5b–d). These surfaces showed several B-induced nanoprecipitates ranging from a few nanometers to tens of nanometers in size. Based on their chemical composition, the B-induced nanoprecipitates in the samples with x = 1, 5, and 10 could be categorized into three types: B-incorporated SiO_x, B-enriched Si-B, and SiB_4 precipitates.

The 3D atom map for x = 1 showed the coexistence of B clusters with Si and O atoms, suggesting the presence of B-incorporated SiO_x ($0.5 \leq x \leq 2$) (Figure 5b). B-incorporated SiO_x nanoprecipitates also existed in the samples with x = 5 and 10, and they were distinguishable from SiO_x particles in samples with x = 0 and 0.2. While SiO_x particles have been observed in Si-Ge alloys,[50,51] the presence of B in SiO_x has not been reported before. The B concentration in SiO_x was ≈10 at.% as shown in the proximity histogram (proxigram), whereas the matrix composition closely matched that of $Si_{80}Ge_{20}$ with ≈0.21 at.% of B (Figure 5e). This observation suggests that when the B concentration exceeds the solubility limit of the Si-Ge matrix, residual B atoms can diffuse into the SiO_x during the high-temperature SPS process. Although B-incorporated SiO_x has been reported in Si used in optical applications, this phase has not been explored for Si or Si-Ge alloys used in thermoelectric applications.[54]

Additionally, distinctive nanoprecipitates primarily composed of Si and B were identified in the samples with x = 1, 5, and 10 (Figure 5f). These precipitates could be differentiated from Si(B) because of their considerably higher B concentration, which ranged from 10–50 at.% (Si_yB, $1 \leq y \leq 10$). However, the amount of B in these precipitates was lower than that required to attain thermodynamic equilibrium (i.e., SiB_n, n = 3, 4, 6, etc.). These metastable Si-B precipitates were previously detected through APT for annealed Si films and referred to as B-enriched clusters.[55] Their compositional variation possibly resulted from uneven diffusion during nonequilibrium fabrication processes. Hereafter, we will refer to these precipitates as B-enriched Si-B. Besides B-incorporated SiO_x and B-enriched Si-B, only the sample with x = 10 contained the SiB_4 equilibrium phase (Figure 5g) since the amount of B was sufficient for the formation of the phase.

While x = 1, 5, and 10 shared common B-induced nanoprecipitates except for SiB_4, the detailed configuration of each nanoprecipitate varied considerably among the different samples. We conducted an in-depth analysis to determine the configurations of nanoprecipitates, focusing on their average size, number density, volume fraction, and composition obtained from APT. To ensure statistical reliability, we employed at least five 3D atom maps for each of the samples with x = 1, 5, and 10, with more than 10 million ions detected. Owing to the irregular shapes of nanoprecipitates in atom maps, we approximated their shape as a sphere with an equivalent volume (the volume enclosed by the 1.5 at.% B iso-concentration surface).

The average size and number density of B-incorporated SiO_x and B-enriched Si-B showed contrasting trends with B concentration. With increasing B concentration, the size of B-incorporated SiO_x increased from 9.1 nm (x = 1) to 13.5 nm (x = 5) and 20.3 nm (x = 10) while the number density decreased (**Figure 6a**). This trend can be attributed to the difference in grain size in each sample. From STEM analyses, the majority of SiO_x particles were located at grain boundaries, suggesting that grain boundaries serve as nucleation sites for SiO_x (Figure S18, Supporting Information). The larger average grain sizes observed in the samples with x = 5 (140.3 nm) and x = 10 (169.5 nm) compared to x = 1 (107.2 nm) indicate a reduced number of nucleation sites for

© 2024 The Authors. Advanced Functional Materials published by Wiley-VCH GmbH
RIGHTSLINK

16163028, 2024, 40, Downloaded from https://onlinelibrary.wiley.com/doi/10.1002/adfm.202403785, Wiley Online Library on [23/10/2024]. See the Terms and Conditions (https://onlinelibrary.wiley.com/terms-and-conditions) on Wiley Online Library for rules of use; OA articles are governed by the applicable Creative Commons License

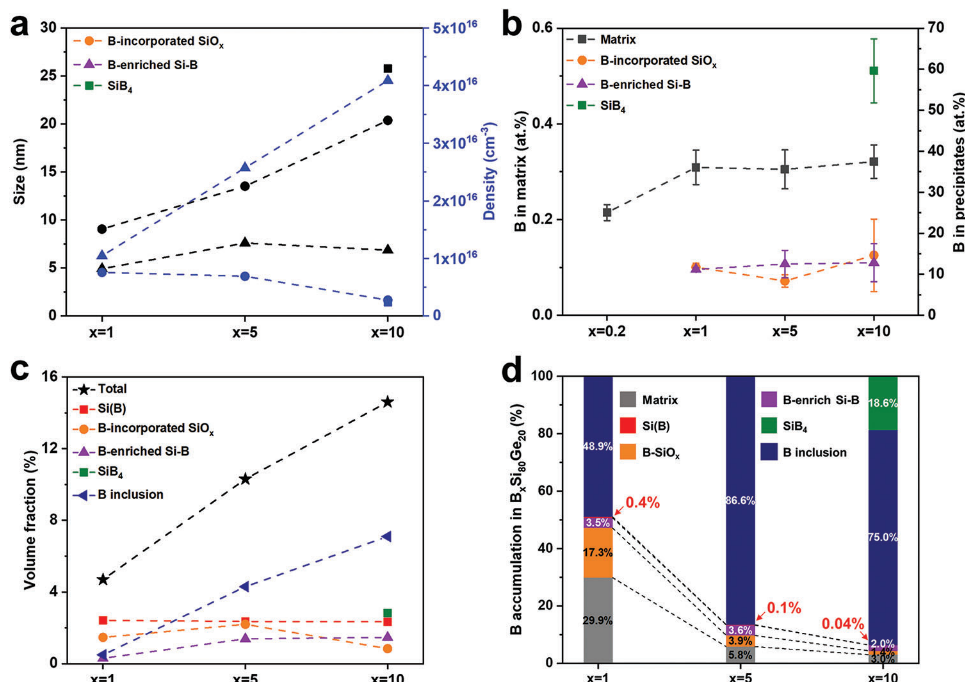

Figure 6. APT results for hierarchical B-induced phases and the holistic distribution of B. a) Size and number density of B-induced nanoprecipitates in the samples with $x = 1$, 5, and 10. b) B concentration in the matrix and nanoprecipitates of samples with $x = 0.2$, 1, 5, and 10, along with the standard deviation. The B concentration in each phase was calculated using the formula [B]/([Si]+[Ge]+[B]), where [A] is the number of A atoms. c) The volume fraction of hierarchical B-induced phases in the samples with $x = 1$, 5, and 10. d) B accumulation chart (unit: percentage) for the samples with $x = 1$, 5, and 10. The dashed lines in (a–d) are for guiding the eyes.

B-incorporated SiO_x particles (Figure S19, Supporting Information). Since total oxygen contents in each sample would be almost identical due to the same fabrication procedure, the number density of B-incorporated SiO_x in the samples with $x = 5$ and $x = 10$ is smaller than $x = 1$ but shows a larger size. These findings suggest that B did not stimulate the nucleation of SiO_x particles but promoted their growth, resulting in larger SiO_x particles in the sample with $x = 10$ compared to the samples with $x = 1$ and 5. This is plausible since SiO_x particles were formed during SPS owing to the presence of residual O in the samples or chamber, regardless of the B concentration. By contrast, the size of B-enriched Si-B precipitates remained almost constant, ranging from 5 to 8 nm, with increasing B concentration (Figure 6a). However, their density increased linearly with B addition, indicating that B promoted the nucleation of B-enriched Si-B precipitates in contrast to the case of B-incorporated SiO_x. The SiB_4 precipitates had the largest average size (≈26 nm) but the smallest number density among the formed nanoprecipitates.

We also compared the average B concentration in the Si-Ge matrix and each nanoprecipitate for the samples (Figure 6b). The matrix B concentration in the sample with $x = 0.2$ was 0.21 at.%, consistent with its p_H. For $x = 1$, 5, and 10, the B concentrations in the matrix were nearly identical (Figure 6b), in good agreement with the p_H values obtained from Hall measurement (Figure 1b). Similarly, the average B concentration of the B-incorporated SiO_x and B-enriched Si-B precipitates remained constant for $x = 1$, 5, and 10, ranging from 11 to 15 at.% (Figure 6b). These results indicate that the addition of B promoted the formation of B-incorporated SiO_x and the nucleation of B-enriched Si-B without significantly increasing the internal B concentration. Notably, SiB_4 in the sample with $x = 10$ showed a much higher B concentration than the other phases.

In addition to the size, number density, and composition, the volume fraction of all B-induced phases was determined through the combined use of XRD and APT. The volume fraction of the Si(B) phase in each sample was obtained through XRD (Figure S9, Supporting Information), while that of B-incorporated SiO_x, B-enriched Si-B, and SiB_4 was obtained from 3D atom maps obtained using APT. However, the volume fraction of B inclusion could not be determined since B inclusion was not detected by XRD and was too large to be entirely included in APT specimens. To calculate the volume fraction of B inclusion, we assumed that the total B concentration of the samples with $x = 1$, 5, and 10 was maintained at a nominal value and that B atoms were distributed among different B-induced phases. Subsequently, we employed the equations

$$N_{total} = \sum_i N_i = \sum_i C_i \times V_i \times \rho_i \tag{3}$$

$$C_{total} \times V_{total} = \sum_i C_i \times V_i \tag{4}$$

(i = matrix, Si(B), B-incorporated SiO_x, B-enriched Si-B, SiB_4, and B inclusion) where N_{total} is the total number of B atoms, and N_i, C_i, V_i, and ρ_i denote the number of B atoms, B concentration, volume fraction, and atomic density per unit volume of each phase (i), respectively. Assuming that ρ_i of the different phases is

© 2024 The Authors. Advanced Functional Materials published by Wiley-VCH GmbH
RIGHTSLINK

roughly identical, we can simplify Equation (3) to Equation (4). By using C_i and V_i of each phase obtained from XRD ($V_{Si(B)}$) and APT analyses, we can then calculate the volume fraction of B inclusion (see Table S2, Supporting Information).

The volume fraction of each phase in the samples with $x = 1$, 5, and 10 is shown in Figure 6c. The Si(B) phase showed a nearly consistent volume fraction, which was obtained from XRD. Similarly, the volume fractions of B-incorporated SiO_x and B-enriched Si-B were similar for $x = 1$, 5, and 10 as their average size and number density showed opposite trends with increasing B concentration. On the other hand, the SiB_4 precipitates showed a slightly higher volume fraction (2.83 vol.%) than Si(B) and the other nanoprecipitates, which can be attributed to their large size. A significant change in the volume fraction with increasing B concentration was observed for the B inclusion. While the volume fraction of the B inclusion was insignificant for $x = 1$ (0.50 vol.%), it increased significantly for $x = 5$ (4.30 vol.%) and 10 (7.10 vol.%) and the B inclusion became the dominant B-induced phase with the highest volume fraction. Consequently, the total volume fraction of all-scale B-induced phases in the samples with $x = 1$, 5, and 10 amounted to 4.70, 10.30, and 14.60 vol.%, respectively (Figure 6c).

Finally, the distribution of B atoms in $B_xSi_{80}Ge_{20}$ was comprehensively visualized by combining the volume fraction of each B-induced phase with the average B concentration of the phase. Figure 6d presents the B accumulation chart that shows the fraction of B atoms in each phase for the samples with $x = 1$, 5, and 10. The chart provides a clear answer to the question raised by the Hall measurements: In which phases do the excess B atoms exist within the Si-Ge matrix? It should be noted that Figure 6d depicts the relative fraction of B atoms in each phase. The B accumulation chart with the absolute B amount is shown in Figure S20 (Supporting Information).

The B accumulation chart shows that the percentage of B atoms in the matrix was 29.9%, 5.8%, and 3.0% for $x = 1$, 5, and 10, respectively. These values are in good agreement with the doping efficiency calculated from the Hall measurement, confirming the reliability of the B accumulation chart (Figure S1, Supporting Information). Furthermore, this result indicates that 70.1%, 94.2%, and 97.0% of B atoms were distributed in the B-induced phases. In the sample with $x = 1$, most of the B atoms were distributed in the B inclusions and B-incorporated SiO_x, while the B inclusion contained the majority of B atoms for $x = 5$. However, for $x = 10$, the B fraction of all existing structures decreased because of the formation of SiB_4 (Figure 6d). Notably, the Si(B) phase contained a very small percentage of B atoms among all the samples (<0.4%) owing to the very low concentration of B in the phase (≈0.15 at.%). This highly heterogeneous distribution of B indicates that a heterogeneous dopant distribution should be considered when modeling thermoelectric materials.

It should be mentioned that in contrast to several reports of grain boundary segregation of B in Si and Si-Ge doped with excess B,[56–58] we did not detect such segregation in any of our samples in the APT analyses. To confirm the absence of B grain boundary segregation, we conducted correlative APT-TEM analyses to verify the existence of grain boundaries in APT specimens before analysis. The sample with $x = 10$ was chosen for the correlative study since it had the highest possibility for showing distinct grain boundary segregation owing to the highest B concentration. From a TEM image, we could identify the presence of a grain boundary at the apex of an APT specimen (Figure S21a, Supporting Information). APT reconstruction of this specimen showed the feature observed in the TEM analysis, thus confirming the presence of a grain boundary in the reconstructed specimen. Importantly, the 3D atom maps revealed B clusters but did not indicate any grain boundary segregation (Figure S21b–d, Supporting Information). The absence of B grain boundary segregation has previously been reported for polycrystalline B-doped Si gates of a MOSFET with an excess amount of B.[59,60] As proposed before, this unexpected B distribution could be attributed to the influence of the synthesis process of Si-Ge or the existence of impurity elements, such as oxygen.[59,61]

2.4. Effect of All-Scale B-Induced Microstructure on Electrical Transport Properties

The formation of the hierarchical B-induced microstructure led to distinctive changes in the electrical transport properties of $B_xSi_{80}Ge_{20}$. The evolution of B-induced phases because of excess B resulted in the saturation of p_H for $x = 1$, 5, and 10 (Figure 1b), as depicted in the B accumulation chart (Figure 6d). This phenomenon was correlated with the unusual variation in m^*, which initially increased up to $x = 1$ but decreased for $x = 5$ and 10, despite of their identical p_H (Figure 1d). To understand this, we investigated the effect of B doping and the resulting B-induced phases on the band structure of $Si_{80}Ge_{20}$. It is well established that $Si_{100-x}Ge_x$ alloys exhibit a Si-like band structure for $x < 85$. Consequently, the band structure of $Si_{80}Ge_{20}$ can be approximated as that of Si, featuring three primary non-parabolic valence bands known as heavy-hole (HH), light-hole (LH), and split-off (SO) bands at the Γ point and a conduction band minimum near the X point.[62] The HH and LH bands degenerate at the Γ point while the SO band is located slightly below the HH and LH (Si: 0.044 eV; Ge: 0.30 eV).[63] Generally, the effect of the SO band on the hole transport of Si-Ge alloys is neglected since their transport properties can be well described by considering only the HH and LH bands.[64] Here, m^* of $Si_{80}Ge_{20}$ can be expressed as[65]

$$m^* = N_V^{2/3}\, m_b^* \tag{5}$$

where N_V and m_b^* are band degeneracy and single band effective mass, respectively.

The introduction of B can create an acceptor level near the valence band, shifting the Fermi level closer to the valence band of Si and $Si_{80}Ge_{20}$.[66] Furthermore, B addition has been reported to increase the DOS of Si, thereby resulting in m^* increasing with the B concentration.[67,68] Likewise, we expected that B addition would also increase the m^* of $Si_{80}Ge_{20}$ alloys and conducted DFT calculations to confirm our hypothesis. The electronic band structure was calculated for pure Si and Si-Ge alloys ($B_{2x}Si_{80-x}Ge_{20-x}$) with varying B doping levels (Figure S22, Supporting Information). From these band structures, we determined the DOS effective mass for holes (m_h^*) and electrons (m_e^*) by differentiating each constituent band of the conduction and valence bands and computing the weighted average mass of each band in different directions (Figure S23, Supporting Information). The result indeed demonstrated an increase in m_h^* with increasing B concentration, while m_e^* unchanged. This finding is consistent with

© 2024 The Authors. Advanced Functional Materials published by Wiley-VCH GmbH
RIGHTSLINK
16163028, 2024, 40, Downloaded from https://onlinelibrary.wiley.com/doi/10.1002/adfm.202403785, Wiley Online Library on [23/10/2024]. See the Terms and Conditions (https://onlinelibrary.wiley.com/terms-and-conditions) on Wiley Online Library for rules of use; OA articles are governed by the applicable Creative Commons License

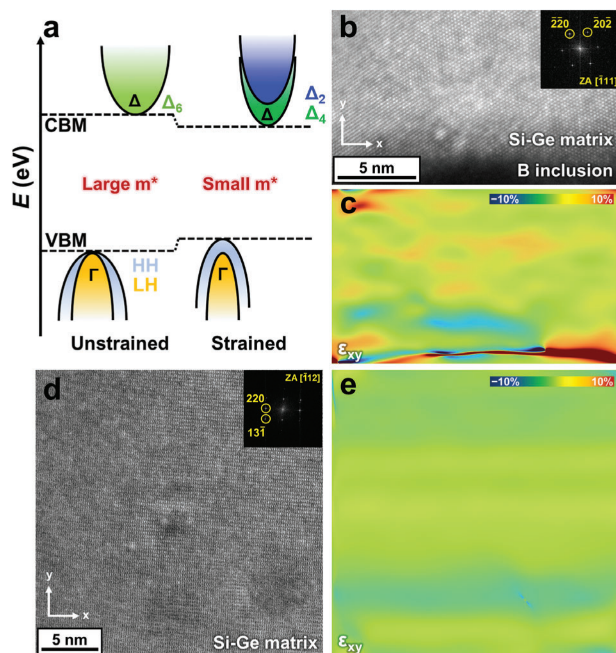

Figure 7. Strain mapping in the sample with $x = 1$ by using geometric phase analysis (GPA). a) A schematic illustrating the potential effect of strain on the band structure of $B_xSi_{80}Ge_{20}$. b–e) A high-resolution HAADF-STEM image and the corresponding strain distribution (ϵ_{xy}) of (b,c) the interface between amorphous B inclusion and Si-Ge matrix and (d,e) Si-Ge matrix far from the B-induced phases obtained through GPA. The insets in (b) and (d) show fast Fourier transform patterns for two diffraction spots selected for use in the GPA.

our result that m^* increased from $x = 0$ to $x = 1$. However, this explanation cannot account for the decrease in m^* for the samples with $x = 5$ and 10 as their DOS would be analogous with that of the sample with $x = 1$ because of the identical p_H. This peculiar m^* reduction can be ascribed to the strain introduced by the B-induced phases. The precipitates in the matrix can create a local strain field when their lattice or volume does not match with the matrix phase.[69] Such strain fields could reduce κ_L by interfering with phonon propagation and even modifying the band structure by altering the original lattice structure of the matrix.[69,70] In the case of Si-Ge, both compressive and tensile strain have been known to break the degeneracy of the valence band by splitting the HH and LH bands and separating the six-fold conduction bands (Δ valleys) into four-fold and twofold bands, resulting in a reduced bandgap and smaller m^* (Schematics in **Figure 7a**).[71,72] Furthermore, strain can impact m_b^* by warping both the conduction and valence band structure of Si and Si-Ge alloys (see Figure 7a).[73,74] Given that μ_H ($\propto 1/m_b^*$) of the sample with $x = 1$ is smaller than that of the $x = 5$ while μ_w ($\propto m^*$) remains comparable in both samples at 298 K, we inferred that the strain field has a more significant effect on m_b^* than N_v.[75] This implies that a reduction in m_b^* due to the band sharpening induced by strain consequently leads to a reduction in m^* for $x = 1$ to $x = 10$.[76,77]

The strain field in $B_xSi_{80}Ge_{20}$ can be originated from both substitutional B in the matrix and B-induced phases. However, since the B concentration in the matrix was almost identical for $x = 1$, 5, and 10, the B-induced phases would be the main factor responsible for the difference in total strain between the samples. The total volume fraction of B-induced phases increased with the nominal B concentration (4.90%, 10.26%, and 14.60% for $x = 1$, 5, and 10, respectively) (Figure 6c). Except for Si(B), which showed a crystalline phase with a coherent interface with the matrix, the other phases (i.e., B-incorporated SiO_x, B-enriched Si-B, SiB_4, and B inclusion) had an amorphous structure. The amorphous-crystalline interface between these phases and the Si-Ge matrix can introduce interfacial lattice strain owing to the density and thermal expansion coefficient mismatch.[31,78] The strain field generated by amorphous B-induced phases was analyzed using high-resolution STEM images and the geometric phase analysis (GPA) method, which is a semiquantitative lattice image processing method.[79] Shear strain mapping (ϵ_{xy}) at the interface between a B inclusion and the Si-Ge matrix showed the presence of a strong strain field at the interface and in the adjacent matrix (Figure 7b,c). By contrast, there was no significant strain in the Si-Ge matrix far from the amorphous B-induced phases (Figure 7d,e). The same trend was obtained for normal strain distributions (ϵ_{xx} and ϵ_{yy}) in both regions (Figure S24, Supporting Information). These results indicate that amorphous B-induced phases generated additional lattice strain in the matrix.

As a larger amount of amorphous B-induced phases was formed with increasing B concentration, the total strain in $B_xSi_{80}Ge_{20}$ also increased. This effect could break the degeneracy of HH and LH bands, leading to reduced m^* for $x = 5$ and 10. Owing to their smaller m^*, the samples with $x = 5$ and 10 exhibited slightly higher μ_H and σ but lower S compared with the sample with $x = 1$ and consequently, they had a smaller PF (Figure 1f). A similar trend in thermoelectric properties (i.e., increased σ and decreased S and PF) has previously been observed in p-type bi-axially strained Si in comparison with unstrained Si under both compressive and tensile strain.[80] This result indicates that the differences in thermoelectric properties between $x = 1$, 5, and 10 in our experiments can be attributed to the effect of strain.

2.5. Effect of All-Scale B-Induced Microstructure on Thermal Transport Properties

The unusual variation in κ_L is also closely linked to the configuration of the B-induced microstructure. As mentioned earlier, the sample with $x = 1$ exhibited much lower κ_L than the samples with $x = 5$ and 10. To investigate the contribution of different phonon scattering mechanisms on κ_L, we used the Debye–Callaway model. We considered five different scattering mechanisms to model κ_L in $B_xSi_{80}Ge_{20}$: Umklapp scattering, alloy scattering, grain boundary scattering, point defect scattering (induced by B atoms), and nanoprecipitate scattering (see details in Supporting Information). The grain size for calculating grain boundary scattering was determined from high-angle annular dark field (HAADF)-STEM images using the line intercept method[81] (Figures S18 and S19, Supporting Information). In particular, for modeling the nanoprecipitate scattering, we only considered B-incorporated SiO_x, B-enriched Si-B, and SiB_4, since Si(B) and B inclusions were much larger (2–4 and 0.5–2 µm, respectively) than the phonon mean free path (i.e., the average distance phonons travel between scattering events) of $Si_{80}Ge_{20}$ alloys (100–300 nm).[30,82] When the size of precipitates significantly

© 2024 The Authors. Advanced Functional Materials published by Wiley-VCH GmbH
RIGHTSLINK
16163028, 2024, 40, Downloaded from https://onlinelibrary.wiley.com/doi/10.1002/adfm.202403785, Wiley Online Library on [23/10/2024]. See the Terms and Conditions (https://onlinelibrary.wiley.com/terms-and-conditions) on Wiley Online Library for rules of use; OA articles are governed by the applicable Creative Commons License

16163028, 2024, 40, Downloaded from https://onlinelibrary.wiley.com/doi/10.1002/adfm.202403785, Wiley Online Library on [23/10/2024]. See the Terms and Conditions (https://onlinelibrary.wiley.com/terms-and-conditions) on Wiley Online Library for rules of use; OA articles are governed by the applicable Creative Commons License

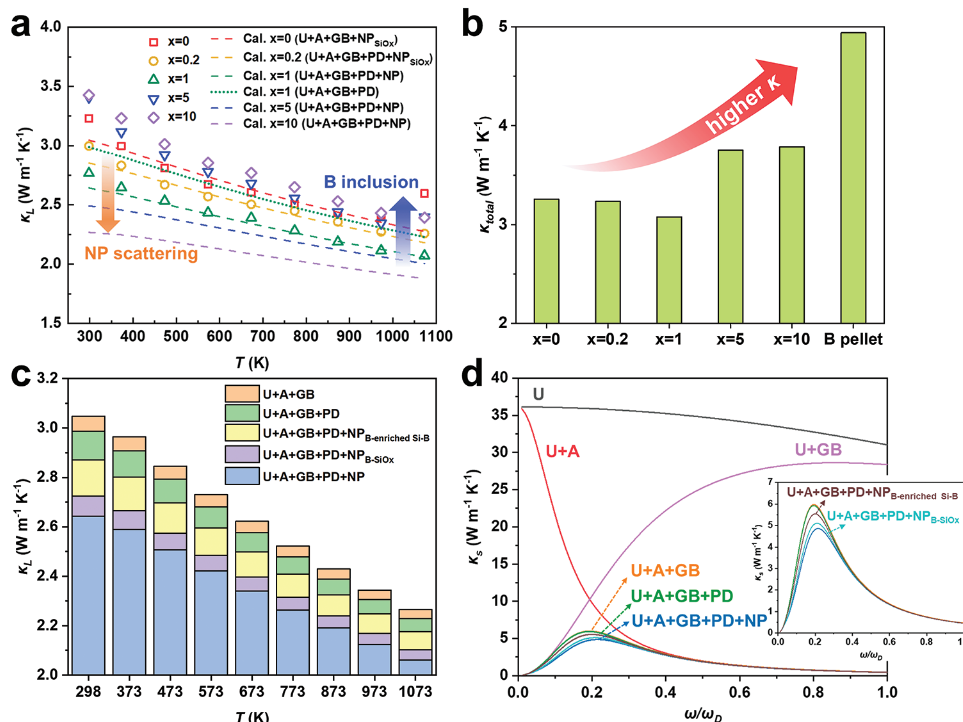

Figure 8. Comparison between experimental κ_L and κ_L calculated using the Debye–Callaway model. a) Temperature-dependent experimental (symbols) and calculated (dashed lines) κ_L for the given scattering mechanisms. b) Comparison of κ_{total} between $B_xSi_{80}Ge_{20}$ and a B pellet measured at 298 K. All samples were fabricated using SPS under identical conditions. c) The contribution of each phonon scattering mechanism to κ_L for $x = 1$ at each temperature. d) The spectral thermal conductivities (κ_s) for $x = 1$ at 298 K for different phonon scattering mechanisms according to the ratio between phonon and Debye frequency (ω/ω_D). The inset shows magnified κ_s excluding U, U+A, and U+GB. Here, U, A, GB, PD, and NP denote Umklapp, alloy, grain boundary, point defect, and nanoprecipitate scattering, respectively. $NP_{B\text{-enriched Si-B (B-SiOx)}}$ denotes nanoprecipitate scattering involving only B-enriched Si-B and B-incorporated SiO_x precipitates.

exceeds the phonon mean free path, phonons do not interact with the feature frequently enough during their propagation, resulting in a limited reduction in κ_{lat}.[83,84] Furthermore, we used the average size, composition, and number density of each nanoprecipitate obtained from APT measurements to model the nanoprecipitate scattering in the Debye-Callaway model (see Table S3, Supporting Information).

The calculated κ_L closely matched the experimental κ_L values for $x = 0$ and 0.2 (**Figure 8a**). With the fitting parameters derived from the samples with $x = 0$ and 0.2, the calculated κ_L for $x = 1$ for nanoprecipitate scattering matched well with the experimental κ_L. By contrast, without considering nanoprecipitate scattering, the calculated κ_L for $x = 1$ was significantly higher than the experimental κ_L (Figure 8a). These findings highlight the substantial role of nanoprecipitates in reducing κ_L for $x = 1$. According to the Debye–Callaway model, the calculated κ_L for $x = 5$ and 10 should be lower than that for $x = 1$, owing to their stronger nanoprecipitate scattering from nanoprecipitates with a higher density. However, such results did not match the experimental κ_L values, which were notably higher by ≈1 W m^{-1} K^{-1}. Considering that the calculated κ_L values for $x = 5$ and 10 without nanoprecipitate scattering were closer to the experimental κ_L, we inferred the existence of a factor that counteracts the decrease in κ_L by nanoprecipitates (Figure S25, Supporting Information).

The main reason behind this discrepancy was identified as the B inclusion, since it is the only B-induced phase that exhibits a significantly different volume fraction between $x = 1$, 5, and 10. To indirectly measure κ_{total} of the B inclusion, we fabricated a B pellet from raw B powder using the same SPS conditions as those for the $B_xSi_{80}Ge_{20}$ samples. Indeed, the B pellet showed a higher κ_{total} (4.94 W $m^{-1}K^{-1}$) than any of the $B_xSi_{80}Ge_{20}$ samples at 298 K (Figure 8b). We report only κ_{total} at 298 K since the B pellet broke at high temperatures owing to insufficient sintering temperature (1273 K) for obtaining a dense B pellet. B powder generally requires 1.5 times higher sintering temperatures (1873–1973 K) than the temperatures we used.[85,86] Nevertheless, it is expected that a denser B pellet would exhibit even higher κ_{total} than the pellet as the density increases. Consequently, the high κ_L of the B inclusion could counterbalance the decrease in κ_L attributed to nanoprecipitate scattering, resulting in the elevated κ_L observed for the samples with $x = 5$ and 10 which had a dominant amount of B inclusions (4.30 and 7.10 vol.%, respectively). By contrast, since the sample with $x = 1$ contained a negligible volume of B inclusions (0.50 vol.%), nanoprecipitate scattering was predominant, leading to lower κ_L. The high κ_{total} of our B pellet conflicts with previous studies that amorphous B reduces κ_L of thermoelectric materials because of its low κ_{total}.[31,87] We presumed that such disparity may be due to Mg impurities in the B inclusion in our samples since κ_{total} of B is very sensitive to the impurity content.[88]

The identical p_H values at 298 K and 1073 K for $x = 1$, 5, and 10 from the high-temperature Hall measurements indicate that

© 2024 The Authors. Advanced Functional Materials published by Wiley-VCH GmbH
RIGHTSLINK

B-induced phases remained stable at high temperatures, and hence they continuously affected the thermal transport properties across the entire temperature range (Figure S3, Supporting Information). Figure 8c shows the contribution of the individual phonon scattering mechanism to κ_L for $x = 1$. It shows that nanoprecipitate scattering suppresses κ_L across all temperatures between 0.2 and 0.4 W m^{-1} K^{-1}. Such reduction in κ_L by nanoprecipitates diminishes with increasing temperature, implying that nanoprecipitate scattering is more dominant at low temperatures. Furthermore, B-incorporated SiO_x was more effective in scattering phonons than B-enriched Si-B precipitates, and hence it suppressed κ_L to a greater extent.

We investigated the contribution of each scattering mechanism based on phonon frequency by calculating spectral thermal conductivities (κ_s) for $x = 1$. The parameter κ_s at 298 K revealed that alloy and grain boundary scattering were major mechanisms for suppressing κ_s and that they were dominant at high ($> 0.3\omega_D$) and low ($< 0.3\omega_D$) frequencies, respectively (Figure 8d). These trends persisted at both temperatures, 673 and 1073 K (Figure S26, Supporting Information). The impact of point defect and nanoprecipitate scattering specifically appeared $\approx 0.2\omega_D$, where a niche area between alloy and grain boundary scattering exists. Furthermore, the suppression of κ_s by B-incorporated SiO_x was more significant than that by point defects and B-enriched Si-B phases, as depicted in Figure 8c. Consequently, κ_s could be reduced across the entire phonon frequency spectrum at all temperatures by the combined contribution of the scattering mechanisms, which corresponds to the concept of "all-scale hierarchical architecture".[25]

3. Conclusion

In summary, we investigate the all-scale hierarchical B-induced microstructures in B-doped $Si_{80}Ge_{20}$ alloys and elucidate their significant impact on thermoelectric transport properties. The combination of multimodal characterization techniques facilitated the identification of five different B-induced phases over a wide length scale along with their microstructural features, including their composition, size, crystal/interface structure, number density, and volume fraction. This detailed information facilitated the mapping of the holistic distribution of B atoms in the $Si_{80}Ge_{20}$ matrix, resulting in the saturation of p_H values. Moreover, by using the GPA and Debye–Callaway model, we show that strain-induced band shifts and contrasting effects of different B-induced phases contributed to atypical variations in m^* and κ_L. These overall effects indicated $x = 1$ to be the optimal carrier concentration with a maximum zT value. Our findings, based on a comprehensive multi-scale characterization approach, not only resolve long-standing questions pertaining to the B-doped Si-Ge alloy system but also underscore the importance of considering all-scale microstructures for accurately determining structure-property relationships in thermoelectric materials. We expect that this approach can be extended to other systems to improve our understanding of the origin of thermoelectric properties and for designing advanced thermoelectric materials.

4. Experimental Section

Fabrication of $B_xSi_{80}Ge_{20}$ and Pure Si Samples: Mechanical alloying and SPS were used to prepare the p-type nanostructured $B_xSi_{80}Ge_{20}$ (x = 0, 0.2, 1, 5, and 10). The stoichiometric amounts of Si chunk (1–4 mm, 99.999%, TAEWON), Ge grains (4–6 mm, 99.99%, TAEWON), and B powder (1–2 um, 99.9%, TAEWON) were loaded in a ball milling jar with tungsten carbide balls. Raw materials were milled in a planetary mill (Nano Ceratech NCTP-05L) at the milling speed set to 300 rpm for 20 h under an argon atmosphere. The as-milled powders were loaded in a 12.7 mm diameter graphite die and consolidated by using SPS (Dr. Sinter Lab SPS-515S, Japan) with the ramping rate of 100 K min^{-1} and sintered for 5 min at 1273 K under 80 MPa. To compare the lattice constant determined by XRD, the sintered pellets of pure Si were synthesized using the identical fabrication process.

Measurement of Thermoelectric Properties: As-sintered samples were cut and polished for thermoelectric property measurement. The σ and S were simultaneously measured from rectangular specimens (3 × 3 × 11 mm^3) using ZEM-3 (Ulvac) with a four-probe method under a He atmosphere. The thermal conductivity of samples was calculated using $\kappa = D\rho C_p$, where D is the thermal diffusivity, ρ is the density, and C_p is the heat capacity. The thermal diffusivity (D) was obtained from disk specimens (Φ 12.7 × 2 mm^3) using LFA-457 (Netzsch). The density of specimens (ρ) was measured by a He gas pycnometer (AccuPyc II 1340, Micromeritics), and the heat capacity (C_p) was determined from the Dulong-Petit law.[89] The average zT (zT_{avg}) value was calculated using the following equation:

$$zT_{avg} = \frac{1}{T_h - T_c} \int_{T_c}^{T_h} zTdT \tag{6}$$

in which T_h and T_c are the temperatures of the hot and cold side, respectively. The uncertainty of zT measurement is between 15 and 20%, due to the combined uncertainty of measuring σ, S, D, ρ, and C_p.[12]

The Hall coefficient (R_H) at room temperature was measured for rectangular specimens (3 × 1 × 9 mm^3) using a Physical Properties Measurements System (PPMS 9T, Quantum Design). The Hall carrier concentration (n) and carrier mobility (μ) were calculated according to the formula $R_H = 1/ne$ and $\sigma = ne\mu$, respectively, with e being the elementary charge. The R_H at room temperature and 1073 K was also measured by HMS model 8407 (Lake Shore Cryotronics Inc.) from cylindrical specimens (Φ 12.7 × 1 mm^3), and the same equations were applied to calculate n and μ.

Measurement of the Sound Velocity: The sound velocities were measured by the pulse-echo method, and a longitudinal transducer (CMR-052, ndtXducer) and a normal incidence shear transducer with a 5 MHz center frequency were utilized for measuring longitudinal (ν_l) and transverse (ν_t) sound velocities, respectively. An ultrasonic pulser/receiver (DPR 300, JSR Ultrasonics) was used for controlling ultrasonic pulse signals, and a digital oscilloscope (DSO-X 2022A, Keysight) was used for recording the signals. The average sound velocity (ν_{avg}) for each specimen was calculated by the following equation from transverse (ν_t) and longitudinal (ν_l) sound velocity.[90]

$$\nu_{avg} = \left[\frac{1}{3}\left(\frac{2}{\nu_t^3} + \frac{1}{\nu_l^3}\right)\right]^{-\frac{1}{3}} \tag{7}$$

Material Characterizations: Phase identification and structural analyses were performed by XRD (SmartLab, RIGAKU) operated with monochromatic Cu Kα1 radiation (λ = 1.5406 Å) at 0.01° step size. The microstructures of samples were observed by SEM (SU-8230, HITACHI), and STEM-EDS (Talos F200X and Titan Themis 80–300, Thermo Fisher). HAADF-STEM images of the interfaces between the matrix and precipitates as well as 4D STEM data were collected using a Cs-corrected STEM (Titan cubed G2 80–300, Thermo Fisher, Cs-correction for the probe forming lens system). STEM and APT specimens were fabricated using a FIB (Helios Nanolab 450, Thermo Fisher). Strain analyses by GPA method were performed with the software Strain++

© 2024 The Authors. Advanced Functional Materials published by Wiley-VCH GmbH
RIGHTSLINK
16163028, 2024, 40, Downloaded from https://onlinelibrary.wiley.com/doi/10.1002/adfm.202403785, Wiley Online Library on [23/10/2024]. See the Terms and Conditions (https://onlinelibrary.wiley.com/terms-and-conditions) on Wiley Online Library for rules of use; OA articles are governed by the applicable Creative Commons License

(http://jjppeters.github.io/Strainpp/) using high-resolution STEM images with marked reference vectors in Figure 7 and Gaussian masks with $\sigma = 5\,\text{nm}^{-1}$.

APT measurements were carried out using a CAMECA LEAP 5000X HR system under pulsed-laser mode at a base temperature of 50 K, a pulse frequency of 125 kHz, a detection rate of 1%, and a laser pulse energy of 30 pJ. Data analyses were done using the commercial AP Suite software developed by CAMECA instruments. All atom maps were reconstructed according to the standard voltage reconstruction protocol. Correlative APT-TEM analyses were done using the protocols proposed by Herbig et al.[91]

Supporting Information

Supporting Information is available from the Wiley Online Library or from the author.

Acknowledgements

This work was supported by the National Research Foundation of Korea (NRF) [grant number: NRF-2023R1A2C2005298] and Samsung Electronics Co., Ltd. (G01230479). C. Jung is grateful for financial support from the Alexander von Humboldt Foundation.

Conflict of Interest

The authors declare no conflict of interest.

Data Availability Statement

The data that support the findings of this study are available from the corresponding author upon reasonable request.

Keywords

atom probe tomography, dopant-induced microstructure, silicon-germanium, thermoelectric, transmission electron microscopy

Received: March 1, 2024
Revised: April 7, 2024
Published online: April 25, 2024

[1] S. Chu, A. Majumdar, *Nature* **2012**, *488*, 294.
[2] L. E. Bell, *Science* **2008**, *321*, 1457.
[3] G. J. Snyder, E. S. Toberer, *Nat. Mater.* **2008**, *7*, 105.
[4] M. Zebarjadi, K. Esfarjani, M. S. Dresselhaus, Z. F. Ren, G. Chen, *Energy Environ. Sci.* **2012**, *5*, 5147.
[5] Q. Yan, M. G. Kanatzidis, *Nat. Mater.* **2022**, *21*, 503.
[6] R. He, T. Zhu, Y. Wang, U. Wolff, J. C. Jaud, A. Sotnikov, P. Potapov, D. Wolf, P. Ying, M. Wood, Z. Liu, L. Feng, N. P. Rodriguez, G. J. Snyder, J. C. Grossman, K. Nielsch, G. Schierning, *Energy Environ. Sci.* **2020**, *13*, 5165.
[7] Y. Lee, S. H. Lo, C. Chen, H. Sun, D. Y. Chung, T. C. Chasapis, C. Uher, V. P. Dravid, M. G. Kanatzidis, *Nat. Commun.* **2014**, *5*, 3640.
[8] G. Joshi, H. Lee, Y. Lan, X. Wang, G. Zhu, D. Wang, R. W. Gould, D. C. Cuff, M. Y. Tang, M. S. Dresselhaus, G. Chen, Z. Ren, *Nano Lett.* **2008**, *8*, 4670.
[9] C. Jung, B. Dutta, P. Dey, S. jae Jeon, S. Han, H. M. Lee, J. S. Park, S. H. Yi, P. P. Choi, *Nano Energy* **2021**, *80*, 105518.
[10] Y. Pei, H. Wang, G. J. Snyder, *Adv. Mater.* **2012**, *24*, 6125.
[11] Y. Yu, D. S. He, S. Zhang, O. Cojocaru-Mirédin, T. Schwarz, A. Stoffers, X. Y. Wang, S. Zheng, B. Zhu, C. Scheu, D. Wu, J. Q. He, M. Wuttig, Z. Y. Huang, F. Q. Zu, *Nano Energy* **2017**, *37*, 203.
[12] C. Jung, K. Jang, H. Park, J. Jang, H. Jang, B. Kang, K. Park, S. Zhang, R. B. Villoro, S. D. Park, H. J. Ryu, Y. S. Jung, M. W. Oh, C. Scheu, S. H. Yi, P. P. Choi, *J. Mater. Sci. Technol.* **2023**, *165*, 39.
[13] C. Gayner, K. K. Kar, *Recent advances in thermoelectric materials* **2016**, *83*, 330.
[14] J. A. Grovogui, T. J. Slade, S. Hao, C. Wolverton, M. G. Kanatzidis, V. P. Dravid, *J. Mater. Res.* **2021**, *36*, 1272.
[15] G. S. Polymeris, N. Vlachos, A. U. Khan, E. Hatzikraniotis, C. B. Lioutas, A. Delimitis, E. Pavlidou, K. M. Paraskevopoulos, T. Kyratsi, *Acta Mater.* **2015**, *83*, 285.
[16] N. Chen, F. Gascoin, G. J. Snyder, E. Müller, G. Karpinski, C. Stiewe, *Appl. Phys. Lett.* **2005**, *87*, 171903.
[17] G. Bai, Y. Yu, X. Wu, J. Li, Y. Xie, L. Hu, F. Liu, M. Wuttig, O. Cojocaru-Mirédin, C. Zhang, *Adv. Energy Mater.* **2021**, *11*, 2102012.
[18] C. Jung, S. jae Jeon, S. Lee, H. Park, S. Han, J. Oh, S. H. Yi, P. P. Choi, *J. Alloys Compd.* **2023**, *962*, 171191.
[19] K. Fang Hsu, S. Loo, F. Guo, W. Chen, J. S. Dyck, C. Uher, T. Hogan, E. K. Polychroniadis, M. G. Kanatzidis, *Science* **2004**, *303*, 818.
[20] K. Biswas, J. He, Q. Zhang, G. Wang, C. Uher, V. P. Dravid, M. G. Kanatzidis, *Nat. Chem.* **2011**, *3*, 160.
[21] C. Jung, S. Zhang, K. Jang, N. Cheng, C. Scheu, S. H. Yi, P. P. Choi, *ACS Appl. Mater. Interfaces* **2023**, *15*, 46064.
[22] S. Abbey, H. Jang, B. Frimpong, N. Kumar, W. H. Nam, V. Q. Nguyen, J. H. Park, C. V. Nguyen, H. Shin, J. Y. Song, S. D. Park, S. Cho, C. Bera, J. Kang, B. G. Park, M. Al Malki, G. J. Snyder, Y. S. Jung, K. H. Hong, M. W. Oh, *Energy Environ. Sci.* **2022**, *16*, 125.
[23] C. Zhang, G. Yan, Y. Wang, X. Wu, L. Hu, F. Liu, W. Ao, O. Cojocaru-Mirédin, M. Wuttig, G. J. Snyder, Y. Yu, *Adv. Energy Mater.* **2023**, *13*, 2203361.
[24] R. Bueno Villoro, D. Zavanelli, C. Jung, D. A. Mattlat, R. Hatami Naderloo, N. Pérez, K. Nielsch, G. J. Snyder, C. Scheu, R. He, S. Zhang, *Adv. Energy Mater.* **2023**, *13*, 2204321.
[25] K. Biswas, J. He, I. D. Blum, C. I. Wu, T. P. Hogan, D. N. Seidman, V. P. Dravid, M. G. Kanatzidis, *Nature* **2012**, *489*, 414.
[26] R. D. Nasby, E. L. Burgess, *J. Appl. Phys.* **1972**, *43*, 2908.
[27] V. S. Shukla, D. M. Rowe, *physica status solidi(a)* **1981**, *66*, 243.
[28] O. Muthusamy, S. Singh, K. Hirata, K. Kuga, S. K. Harish, M. Shimomura, M. Adachi, Y. Yamamoto, M. Matsunami, T. Takeuchi, *ACS Appl Electron Mater* **2021**, *3*, 5621.
[29] J. Mackey, F. Dynys, A. Sehirlioglu, *Acta Mater.* **2015**, *98*, 263.
[30] A. J. Minnich, H. Lee, X. W. Wang, G. Joshi, M. S. Dresselhaus, Z. F. Ren, G. Chen, D. Vashaee, *Phys Rev B* **2009**, *80*, 155327.
[31] G. Yang, R. Niu, L. Sang, X. Liao, D. R. G. Mitchell, N. Ye, J. Pei, J. F. Li, X. Wang, *Adv. Energy Mater.* **2020**, *10*, 2000757.
[32] W. Gao, X. Yi, B. Cui, Z. Wang, J. Huang, J. Sui, Z. Liu, *J Mater Chem C Mater* **2018**, *6*, 9821.
[33] M. Kubouchi, K. Hayashi, Y. Miyazaki, *Scr. Mater.* **2016**, *123*, 59.
[34] R. W. Olesinski, G. J. Abbaschian, *Bulletin of alloy phase diagrams* **1984**, *5*, 478.
[35] C. S. Witharamage, J. Christudasjustus, R. K. Gupta, *J. Mater. Eng. Perform.* **2021**, *30*, 3144.
[36] C. Jacoboni, C. Canali, G. Ottaviani, A. Quaranta, *Solid State Electron* **1977**, *20*, 77.
[37] D. Thompson, D. Hitchcock, A. Lahwal, T. M. Tritt, *Emerging Materials Research* **2012**, *1*, 299.
[38] A. Lahwal, X. Zeng, S. Bhattacharya, M. Zhou, D. Hitchcock, M. Karakaya, J. He, A. M. Rao, T. M. Tritt, *Energies (Basel)* **2015**, *8*, 10958.
[39] F. Li, X. Liu, N. Ma, L. Chen, L. M. Wu, *Angewandte Chemie – International Edition* **2022**, *134*, 202208216.
[40] J. P. Heremans, V. Jovovic, E. S. Toberer, A. Saramat, K. Kurosaki, A. Charoenphakdee, S. Yamanaka, G. J. Snyder, *Science* **2008**, *321*, 554.

© 2024 The Authors. Advanced Functional Materials published by Wiley-VCH GmbH

RIGHTSLINK

16163028, 2024, 40, Downloaded from https://onlinelibrary.wiley.com/doi/10.1002/adfm.202403785, Wiley Online Library on [23/10/2024]. See the Terms and Conditions (https://onlinelibrary.wiley.com/terms-and-conditions) on Wiley Online Library for rules of use; OA articles are governed by the applicable Creative Commons License

[41] S. Dongmin Kang, G. Jeffrey Snyder, *Nat. Mater.* **2017**, *16*, 252.
[42] L. Wu, J. Yang, M. Chi, S. Wang, P. Wei, W. Zhang, L. Chen, J. Yang, *Sci. Rep.* **2015**, *5*, 14319.
[43] G. J. Snyder, A. H. Snyder, M. Wood, R. Gurunathan, B. H. Snyder, C. Niu, *Adv. Mater.* **2020**, *32*, 2001537.
[44] K. W. Shin, S. Song, H. W. Kim, G. Do Lee, E. Yoon, *Jpn. J. Appl. Phys.* **2018**, *57*, 065504.
[45] R. B. Stein, The thermal conductivity of boron. Master Thesis, Oregon State University, Corvallis USA **1954**.
[46] U. Anselmi-Tamburini, Y. Kodera, M. Gasch, C. Unuvar, Z. A. Munir, M. Ohyanagi, S. M. Johnson, *J. Mater. Sci.* **2006**, *41*, 3097.
[47] H. Zhang, B. N. Kim, K. Morita, H. Yoshida, K. Hiraga, Y. Sakka, *J. Am. Ceram. Soc.* **2011**, *94*, 3206.
[48] C. B. Vining, W. Laskow, J. O. Hanson, R. R. Van Der Beck, P. D. Gorsuch, *J. Appl. Phys.* **1991**, *69*, 4333.
[49] B. A. Cook, J. L. Harringa, S. H. Han, B. J. Beaudry, *J. Appl. Phys.* **1992**, *72*, 1423.
[50] G. Bernard-Granger, K. Favier, M. Soulier, C. Navone, M. Boidot, B. Deniau, P. Grondin, J. Leforestier, J. Simon, *Scr. Mater.* **2014**, *93*, 40.
[51] A. Usenko, D. Moskovskikh, M. Gorshenkov, A. Voronin, A. Stepashkin, S. Kaloshkin, D. Arkhipov, V. Khovaylo, *Scr. Mater.* **2017**, *127*, 63.
[52] B. Gault, M. P. Moody, J. M. Cairney, S. P. Ringer, *Atom probe microscopy*, Vol. *160*, Springer Science & Business Media, Berlin **2012**.
[53] B. Gault, A. Chiaramonti, O. Cojocaru-Mirédin, P. Stender, R. Dubosq, C. Freysoldt, S. K. Makineni, T. Li, M. Moody, J. M. Cairney, *Nature Reviews Methods Primers* **2021**, *1*, 51.
[54] D. Hiller, J. López-Vidrier, S. Gutsch, M. Zacharias, M. Wahl, W. Bock, A. Brodyanski, M. Kopnarski, K. Nomoto, J. Valenta, D. König, *Sci. Rep.* **2017**, *7*, 8337.
[55] O. Cojocaru-Miŕdin, D. Mangelinck, D. Blavette, *J. Appl. Phys.* **2009**, *106*, 113525.
[56] H. Watanabe, M. Tamura, M. Dainin, M. Seto, H. Katoh, K. Taniguchi, *Jpn. J. Appl. Phys.* **2003**, *42*, 1937.
[57] B. Han, H. Takamizawa, Y. Shimizu, K. Inoue, Y. Nagai, F. Yano, Y. Kunimune, M. Inoue, A. Nishida, *Appl. Phys. Lett.* **2015**, *107*, 023506.
[58] Y. Tu, H. Takamizawa, B. Han, Y. Shimizu, K. Inoue, T. Toyama, F. Yano, A. Nishida, Y. Nagai, *Ultramicroscopy* **2017**, *173*, 58.
[59] H. Takamizawa, Y. Shimizu, K. Inoue, Y. Nozawa, T. Toyama, F. Yano, M. Inoue, A. Nishida, Y. Nagai, *Appl. Phys. Express* **2016**, *9*, 106601.
[60] K. Inoue, F. Yano, A. Nishida, H. Takamizawa, T. Tsunomura, Y. Nagai, M. Hasegawa, *Ultramicroscopy* **2009**, *109*, 1479.
[61] K. Nomoto, H. Sugimoto, X. Y. Cui, A. V. Ceguerra, M. Fujii, S. P. Ringer, *Acta Mater.* **2019**, *178*, 186.
[62] N. Mori, Silicon–Germanium (SiGe) Nanostructures, **2011**, 26.
[63] M. O. Baykan, S. E. Thompson, T. Nishida, *J. Appl. Phys.* **2010**, *108*, 093716.
[64] C. B. Vining, MRS Online Proceedings Library (OPL) **1991**, *234*.
[65] Y. Pei, H. Wang, G. J. Snyder, *Band engineering of thermoelectric materials* **2012**, *24*, 6125.
[66] A. Souifi, G. Brémond, T. Benyattou, G. Guillot, D. Dutartre, P. Warren, *Appl. Phys. Lett.* **1993**, *62*, 2986.
[67] H. D. Barber, *Solid State Electron* **1967**, *10*, 1039.
[68] H. M. Van Driel, *Appl. Phys. Lett.* **1984**, *44*, 617.
[69] J. He, J. R. Sootsman, S. N. Girard, J. C. Zheng, J. Wen, Y. Zhu, M. G. Kanatzidis, V. P. Dravid, *J. Am. Chem. Soc.* **2010**, *132*, 8669.
[70] D. Narducci, S. Frabboni, X. Zianni, *J. Mater. Chem. C* **2015**, *3*, 12176.
[71] D. J. Paul, *Adv. Mater.* **1999**, *11*, 191.
[72] A. Druzhinin, I. Ostrovskii, Y. Khoverko, N. Liakh-Kaguy, V. Mazur, *Applied Nanoscience (Switzerland)* **2022**, *12*, 913.
[73] S. Richard, N. Cavassilas, F. Aniel, G. Fishman, *J. Appl. Phys.* **2003**, *94*, 5088.
[74] S. K. Chun, *Strain effects on the transport and optical properties of the SiGe alloy*, University of California, Los Angeles, **1992**.
[75] J. He, Y. Xia, S. S. Naghavi, V. Ozoliņš, C. Wolverton, *Nat. Commun.* **2019**, *10*, 719.
[76] M. V. Fischetti, S. E. Laux, *J. Appl. Phys.* **1996**, *80*, 2234.
[77] B. Senapati, *IETE J Res* **2007**, *53*, 215.
[78] G. Wu, X. Han, J. Cai, P. Yin, P. Cui, X. Zheng, H. Li, C. Chen, G. Wang, X. Hong, *Nat. Commun.* **2022**, *13*, 4200.
[79] L. Fu, K. H. Lee, S. Il Kim, J. H. Lim, W. Choi, Y. Cheng, M. W. Oh, Y. M. Kim, S. W. Kim, *Acta Mater.* **2021**, *215*, 117058.
[80] N. F. Hinsche, I. Mertig, P. Zahn, *Journal of Physics Condensed Matter* **2011**, *23*, 295502.
[81] P. A. P. Moran, S. K. RoY, Linear Intercepts, Areas and Volumes IN recent correspondence Amplitude Effect in Cepheid Variables, Vol. *155*, **1945**.
[82] Y. Lan, A. J. Minnich, G. Chen, Z. Ren, *Adv. Funct. Mater.* **2010**, *20*, 357.
[83] N. Mingo, D. Hauser, N. P. Kobayashi, M. Plissonnier, A. Shakouri, *Nano Lett.* **2009**, *9*, 711.
[84] X. Yang, J. Carrete, Z. Wang, *Appl. Phys. Lett.* **2016**, *108*, 113901.
[85] Y. Takagiwa, N. Kuroda, E. Imai, I. Kanazawa, H. Hyodo, K. Soga, K. Kimura, *Mater. Trans.* **2016**, *57*, 1066.
[86] H. Kim, K. Kimura, *Mater. Trans.* **2011**, *52*, 41.
[87] H. Wang, G. Wu, Z. Yan, X. Tan, J. Cai, H. Hu, P. Sun, G. Liu, J. Jiang, *Chem. Eng. J.* **2021**, *420*, 130381.
[88] D. G. Cahill, H. E. Fischer, S. K. Watson, R. O. Pohl, G. A. Slack, *Phys. Rev. B* **1989**, *40*, 3254.
[89] D. P. Louis, P. Alexis-Thérèse, Chimie. Physique.**1819, 10, 395**.
[90] H. Jang, M. Y. Toriyama, S. Abbey, B. Frimpong, J. P. Male, G. J. Snyder, Y. S. Jung, M. W. Oh, *Adv. Mater.* **2022**, *34*, 2204132.
[91] M. Herbig, P. Choi, D. Raabe, *Ultramicroscopy* **2015**, *153*, 32.

© 2024 The Authors. Advanced Functional Materials published by Wiley-VCH GmbH
RIGHTSLINK
16163028, 2024, 40, Downloaded from https://onlinelibrary.wiley.com/doi/10.1002/adfm.202403785, Wiley Online Library on [23/10/2024]. See the Terms and Conditions (https://onlinelibrary.wiley.com/terms-and-conditions) on Wiley Online Library for rules of use; OA articles are governed by the applicable Creative Commons License